REPRESENTATIVE TEST RESULTS FROM HELINOVI AEROACOUSTIC MAIN ROTOR/TAIL ROTOR/FUSELAGE TEST IN DNW

Jianping Yin, Berend Van der Wall(1), Stefan Oerlemans(2) et al.
DLR, Institute of Aerodynamics and Flow Technology, Germany
1) DLR, Institute of Flight Systems, Germany
2) National Aerospace Laboratory NLR, The Netherlands

Abstract

In the framework of the European HeliNOVI project, an acoustic DNW wind tunnel study was conducted into helicopter tail rotor noise. The goal of the tests was to investigate (1) the importance of tail rotor noise for different flight conditions (2) main rotor/tail rotor interaction noise, and (3) tail rotor noise reduction concepts. Besides the conventional measurement techniques, such as an inflow microphone traverse, blade pressure transducers and PIV, an out-of-flow phased microphone array was applied to locate and quantify the different helicopter noise sources. The test results indicate that tail rotor noise is most important for climb and high-speed level flight. Furthermore, it is found that main rotor/tail rotor interactions only have a small effect on the overall noise levels. After a reduction of rotor tip speed, the most efficient tail rotor noise reduction concept involves changing the tail rotor sense of rotation from 'advancing side down' to 'advancing side up'.

1. Introduction

The helicopter is a versatile means of transport and fulfills increasingly a unique role in civil and military aviation, but a negative undesirable by-product of the helicopter during its operation is noise generation. The main sources of helicopter noise are its main rotor (MR), tail rotor (TR), engine, and the drive-train components. The dominant noise contributors are the MR and the TR since they operate in free atmosphere and thus radiate noise unobstructed into the surroundings. With rising concern for environmental issues and increasingly stringent noise regulation, helicopter noise has gained importance in comparison to performance, safety and reliability.

The main research effort in the past was concentrated on the reduction of MR noise, where extensive work, both theoretical and experimental helped to deepen the understanding of the mechanisms of the generation and reduction of MR noise such as recent work reported in [Ref.1]. Even though the TR has long been recognized as a significant source of helicopter noise [Ref.2~8], research effort towards tail rotor noise reduction has been less. The reason is that the complex flow surrounding the TR poses an extreme challenge for both experimental and theoretical study. The flow around TR is the result of the interaction of flows generated by the MR wake, fuselage, rotor hub, engine exhaust and empennage flows in addition to its own wake. In order to improve the understanding of TR noise generation and mechanisms for its reduction, especially the TR noise under the influence of MR and fuselage, etc, detailed information on both the radiated sound field and the characteristics of the unsteady blade pressures together with the flow field around TR are crucial and necessary. This information can also be used to validate prediction tools for TR noise, including the effects of MR/TR interactions, suitable for future aircraft design and retrofit purposes. However such essential database is presently unavailable within European helicopter noise research community.

The EU HeliNOVI project is designed to resolve the deficiency in TR noise data and is part of the continuing EU effort towards improving the understanding of TR noise reduction and vibration reduction technology by means of a comprehensive investigation of MR/TR interaction noise and rotor induced vibrations through both theory and experiment. The research goal of HeliNOVI is to provide new validated design codes and technologies for reducing the noise and vibration of rotary wing aircraft. In addition, a unique database of high resolution airloads on rotor blades and fuselage and of the radiated noise levels can be generated.

A comprehensive experimental program within HeliNOVI was launched employing 40% geometric and dynamic scaled helicopter wind-tunnel model. The whole wind tunnel test is divided into two parts, an aeroacoustic test and a vibration test.

The present paper will only focus on aeroacoustic test. The model is well equipped with densely instrumented MR and TR as well as a lightly instrumented fuselage. To improve the understanding of the effect of MR wake on TR inflow, a 3-component flow visualization and flow velocity measurement, by means of Particle Image Velocimetry (PIV), are also employed on planes near TR inflow and outflow region parallel to the free stream. The acoustic signal is measured by the inflow microphone array (16 Mics) mounted on a traverse. Besides the conventional measurement techniques, a 140-microphone out-of-flow phased array was applied to locate and quantify the different noise sources on the model.

To assess the potential contamination of the rotor signal due to non-physical reflection, a reflection test using small explosive charges was also performed.

The major objectives of acoustic test are to generate an unique high quality aerodynamic and aeroacoustic database for; (1) Validating prediction design tools for TR noise prediction - including main/tail rotor interactions; (2) Establishing the importance of the TR with respect to the overall noise radiation and (3) evaluation of TR noise reduction potentials. The aerodynamic results include high resolution unsteady airloads on rotor blades and fuselage, 3-component flow visualization and PIV around TR inflow and outflow areas to determine the MR tip vortex flow field (velocity vector field) for a few cases of the flight envelope. The acoustic results consist of acoustic time history, spectrum and footprint from inflow and outflow microphones. Although the phased array technique has been used in many aeroacoustic studies already (e.g. airframe noise [Ref.9,10], wind turbine noise [Ref.11,12], and airfoil sections [Ref.13]), its application to helicopter noise has been rather limited [Ref.14,15]. Therefore, in this paper selected results will be presented to illustrate the capabilities of the phased array technique for helicopter noise.

Two set of TR blades are used for different test configurations. The tested configuration in aeroacoustic part address a number of noise reduction techniques; (1) TR sense of rotation (NACA 0012 TR used), (2) Variation of position between MR and TR (S102 TR used), (3) Variation of rotor rotational speed. The flight conditions covered include level, climb, and descent flight at various flight speeds.

This paper first presents the experimental approach; including wind tunnel model, rotor blade characteristics and acoustic instrumentation (inflow microphone traverse and microphone array system), and then provides samples of a small number of representative results together with data analysis, including; (1) inflow microphone measurements, (2) the out-of-flow microphone array results, (3) unsteady blade pressure, (4) vortex detection, i.e. the MR tip vortex flight path through the PIV planes.

2. Test Set-up

2.1 Wind tunnel Facility and Model Description

HeliNOVI wind tunnel test campaign was performed in DNW 8m by 6 m open jet test section known for its excellent flow quality and anechoic properties as well as its low background noise. *Fig.1* presents an overview of the test set up and DLR test rig as well as inflow and outflow microphone system in this wind tunnel.

Fig.1: HeliNOVI *test set up for aeroacoustic test*

The BO105 model consists of dynamically and Mach scaled main rotor blades and a geometrically scaled fuselage including teetering tail rotor system [Ref.16]. More information can also be found in [Ref.17]. The tail rotor flapping is enabled by a central flap hinge with pitch-flap-coupling. The BO105 wind tunnel model is composed of several subsystems. The backbone of the model is the MWM (modular wind tunnel model) containing core components like gear box, rotor shaft and drive train system for the main rotor in a shell. The high modularity of the MWM allows an easy adaptation of the wind tunnel model to the required HeliNOVI configuration by integrating the fuselage shell (including airframe balance), the tail boom (including tail rotor with motor and possibility of new TR position) and the model support into the MWM.

The MWM consists of three major subsystems: the rotor drive system, the rotor balance and the rotor control system. The core of the rotor drive system is a nine piston axial hydraulic motor connected by hydraulic lines to a remotely located electric driven pump. The hydraulic motor drives the rotor shaft via bevel gear (gear ratio 2.2) and offers a power capacity of 130 kW at 1050 rpm. The rotor balance system is a six component balance containing separate measuring elements (in serial arrangement) for static and dynamic load components. The rotor control system is based on a swashplate system consisting of three electrodynamic actuators attached to the fixed system, the swashplate and the rotating blade pitch rods. The computer controlled actuators provide collective and cyclic blade pitch control by moving the non-rotating part of the swashplate in the desired way.

2.2 Rotor and Fuselage Instrumentation

In all 118 dynamic pressure sensors are used of which 51 are on MR, 36 on TR and 31 on fuselage, tail boom and stabilizers (vertical and horizontal).

2.2.1 MR instrumentation

The MR is a geometrically and dynamically scaled model of the four-bladed hingeless BO105 MR with a NACA23012 airfoil whose trailing edge was modified to form a 5 mm long tab in order to match the geometry of the full scale rotor. The rotor has a diameter of 4 m with a root cut-out of 0.35 m and a chord length of 0.121 m. The blades have a linear twist of –8 deg (–4 deg/m) and a rectangular plan form leading to a solidity of 0.077.

Two blades of the MR, named “red” and “yellow” are instrumented with 25 and 26 Kulite pressure transducers respectively. The numbering of the sensors is given in *Fig. 2*. On the “yellow” blade, radial station at 87% is instrumented with 17 sensors, whereas the remaining 6 are located at 4 stations. The sensors on the “red” blade are distributed as follows: 8 at 87%, 4 at 88% and 86% and 2 at 81%, 83%, 85%, 92% and 97%. These two sets offer:

- A fully instrumented station at 87%
- An indication at stations 40, 60, 75, 81, 83, 85, 86,88, 92 and 97%
- In detail the region of the leading edge at 87%, and
- An opportunity to detect any differences between the blades at stations 87% and 97%

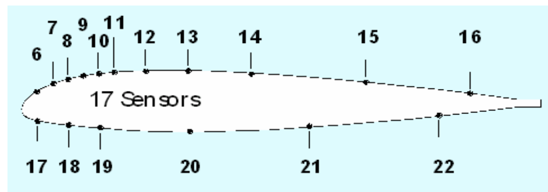

(a)The numbering of the sensors at the 87% section of the MR “yellow” blade

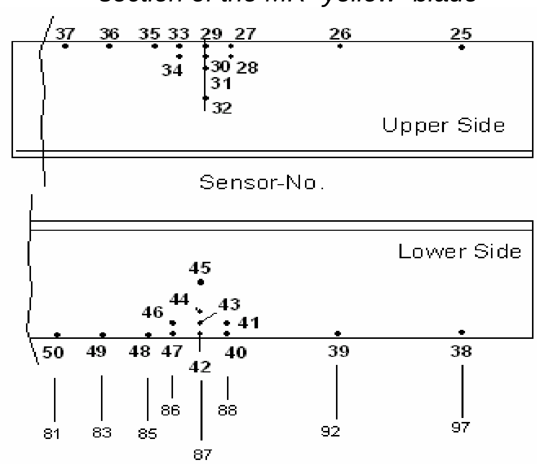

(b) The numbering of the sensors at the MR “red” blade

Fig. 2: Example of the sensors on the MR blade

2.2.2 TR instrumentation

The TR of the HeliNOVI wind tunnel model is a geometrically scaled model of the two-bladed BO105 see-saw TR. The TR blades have no twist and a standard square tip. Two set of TR blades are used each with one blade instrumented. As shown in *Fig.3* and *4*, TR S102 blade has 36 sensors, and TR NACA0012 blade has 20 sensors.

The NACA blade is employed to study the effects of different TR rotational direction.

On the TR_S102 blade, stations at r/R=0.8 and 0.97 are well equipped and the pressure at the leading edge is provided at 4 more radial stations. The TR_NACA012 blade has only the 97% station well instrumented with indication of the pressure at the leading edge provided at three more stations.

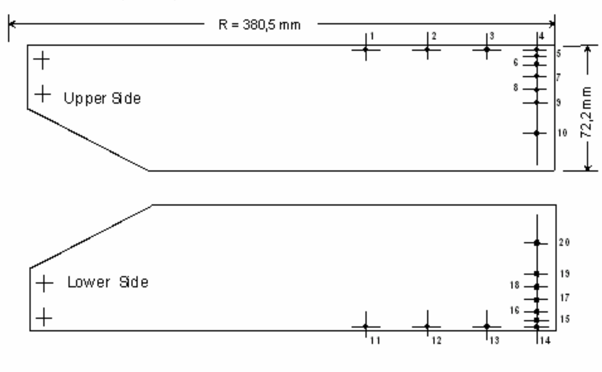

Fig.3 The numbering of sensors on the TR_NACA012 blade

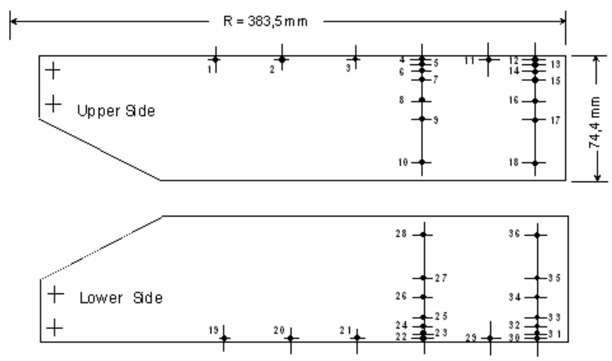

Fig. 4: The numbering of sensors on the TR S102 blade

2.2.3 Fuselage Instrumentation

Regarding state-of-the-art modeling techniques, the design and manufacture of a dynamically scaled helicopter fuselage is beyond conventional helicopter wind tunnel model technology. Therefore, only geometric similarity of the fuselage is considered for the BO105 wind tunnel model. Pressure is also measured on the fuselage at 31 locations including sensors on tail boom, horizontal stabilizer and tail fin.

2.3 Stereo PIV measurement set-up

In order to cover the measurement locations of the proposed test matrix , a common support was used that had three traverses (7.6m in x, 2.1m in y, and 1.7m in z direction) plus a central hinge for rotations about the vertical axis, see *Fig. 5*. On the lower platform two double-pulse Nd:YAG lasers (2x320 mJ each) were mounted, their beams were directed vertically into the flow and aligned on the same plane with a thickness of 7mm, for maximum light energy. The camera systems were mounted on the z-traverse of the common support's vertical tower such that the entire tail rotor area could be measured. In this setup, the vertical distance between the cameras was 7.1m and the horizontal distance to the light sheet could be kept constant at 5.7m during all PIV measurements. Therefore, a pixel-to-length re-calibration and camera alignment (which usually has to be performed after each change in the setup) could be avoided. Di-Ethyl-Hexyl-Sebacat (DEHS) atomized by Laskin nozzle particle generators was used to seed the flow. The particles were pumped through a distribution rake mounted in the settling chamber of the wind tunnel. The rake was remotely traversed to guide the homogeneous seed stream to the region of interest. The DEHS droplets generated and distributed by this arrangement have a mean diameter below 1µm as confirmed by previous tests. Inside the tip vortex the seeding density is noticeably lower than in the remainder of the flow field. This can be explained by the reduced air density inside the core and centrifugal forces that effect the particle distribution.

The CCD cameras (1280x1024 pixel resolution, 12bit grey scale) had 135mm lenses and were spaced vertically such that one camera was looking from below the observation area, and the other camera from above. One measurement plane was located on the suction side of the tail rotor 108mm away from the disk and the second plane was located on the blowing side 52mm away from the disk, as shown in *Fig.6*. One example of flow visualization from one PIV window for 12° climb at 33m/s case is given in *Fig.7*.

The PIV trigger was synchronized to the MR azimuth from 0deg to 150deg in increments of 30deg. Thus, the MR tip vortex flight path through the TR disk was covered. Five positions of the observation area, with some overlap, were selected to cover the entire TR area, except where the horizontal stabilizer and its end plates prohibited measurements. The observation area covered 378mm horizontally (almost the TR radius of 383mm) and 339mm vertically.

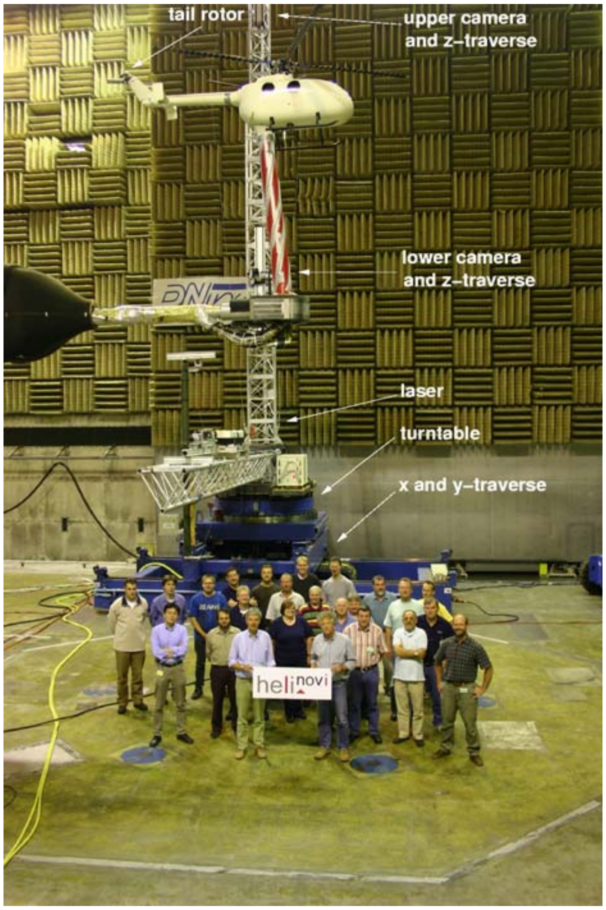

Fig. 5: Test set-up for PIV measurements in the TR area

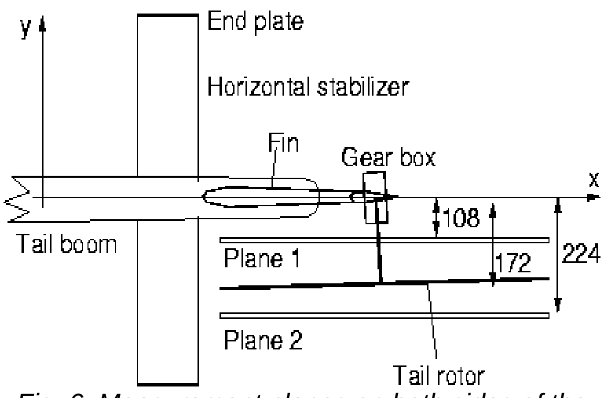

Fig. 6: Measurement planes on both sides of the TR (right, top view)

Fig.7: One example of flow visualization from one PIV window for 12° climb case (wind comes from right side)

2.4 Acoustic instrumentation

Acoustic measurements were made both inside and outside the wind tunnel flow. The inflow measurements were done using 16 ½-inch microphones mounted on a U-shaped wing support (*Fig.1*). The microphones were aligned with the tunnel axis and were pointing upstream. The wing support was lined with foam to suppress reflections, and was traversed in streamwise direction in steps of 0.5 m. The vertical distance between the main rotor hub and the horizontal part of the wing support was in most cases 2.3 m.

The out-of-flow phased array consisted of 140 ½-inch microphones in an open metal grid of 4mx4m, and was fixed to the inflow microphone traverse (*Fig.1*). The microphones had wind screens to prevent flow-induced noise. The vertical distance between the microphones and the center of the MR was typically 7.15 m, and the lateral distance between the array center and the tunnel centerline was 0.5 m. Array measurements were generally performed for two streamwise positions: directly below the model and 4.2 m upstream.

2.5 Test procedure, trim and MR/TR configuration

At the beginning of each new configuration the inflow microphone traverse is moved to its most upstream position. The rotor conditions are then adjusted by DLR and the wind tunnel conditions by DNW. After the conditions are reached, the performance data of the rotors are measured, followed by blade pressure measurements and finally acoustic measurements. The blade pressure data was synchronized with 1P MR signal while simultaneously storing 1P TR signal as well as MR and TR blade azimuth position signals for identifying relative position of MR and TR. Two different data acquisition modes, A-mode and B-mode are used for acoustic inflow microphone data. In A-mode, the data acquisitions are synchronized with the 1P of both MR and TR signal while in B-mode, or free-running-mode, measurements are not locked to the rotor rotation. The data averaging of acoustic signal was trigged either by 1P of MR or by 1P of TR, depending on the required data analysis.

During tests, the rotors are trimmed to prescribed helicopter weight and MR hub-moments. This trim procedure allows having the same trimmed values as those used in pre-test predictions performed within the project. The prescribed values have been pre-calculated by ECD using the STAN code which is a flight mechanics code. During the test TR thrust is the result of the trim procedure. The tests are first started with both MR and TR in operation in order to obtain TR thrust which was then used for the isolated TR case.

The test matrix comprised of flight conditions such as climb, descent and level flight with different flight speeds. The tested configuration included; (1) MR+TR as well as isolated MR and isolated TR; (2) Tail rotor sense of rotation (NACA 0012 TR used); (3) Variation of relative position of main rotor and tail rotor, (4) Variation of rotor rotational speed.

3. Data Acquisition and Processing

One of main objective of this test campaign is to generate a suitable data base for code validation by measuring a comprehensive set of acoustical and blade pressure data as well as the flow field (PIV). This set of data also includes related test conditions of the rotor system and wind tunnel operational data. The ratio of TR and MR rotational speed is chosen as 5 instead of 5.3 from original BO105 in order to match that used in pre-test prediction. The reason for choosing an integer RPM ratio in pre-test prediction is to reduce simulation time for capturing the periodicity of the MR and TR interaction. This integer value can't, however, be strictly fulfilled during test as the driving systems of MR and TR are not synchronized mechanically. Therefore, extra effort is required for doing the data averaging.

3.1 Aerodynamic Data

For analysis purposes, Cp vs. chordwise location at specified times (azimuth angles) and averaged over one MR or TR revolution as well as time history of Cp for specified sensors are available on line. For data post processing, a further and probably more meaningful approach to demonstrate the interference effect of MR wake on TR aerodynamic behavior is to perform TR data averaging over 5 TR revolutions instead of 1 TR revolution, since the ratio of TR and MR rotational speed is chosen as 5 during the test. As mentioned previously, due to the possible fluctuation of MR and TR rotational speed as well as non-synchronized MR/TR driving system, the relative azimuth positions of MR and TR is arbitrary. The phasing may be important for integer-multiple RPM during averaging. Therefore not all TR blade pressure data could be used in the averaging. The searching TR blade pressure data with same MR and TR starting azimuth angle for the averaging is necessary. *Fig.8* demonstrates the MR azimuth angles as function of TR revolutions which are counted when TR reference blade points downstream ($\psi_{TR} = 0.0$) for the 12° climb case. The step size of TR revolution in the plot is 5 in correlation with ratio of MR/TR RPM. The figure shows that reference MR blade does not return to its initial azimuth position (55.5°) after every 5 TR revolutions. The observed variation is about 13° for current case. A special code is developed to define all possible TR revolutions which can be used for the averaging for a given variation tolerance of MR azimuth angle $\Delta\psi_{MR}$. A $\Delta\psi_{MR} = 5^o$ is chosen for all following data reduction. *Fig.8b* gives an example of selected revolutions when MR $\Delta\psi_{MR} = 5^o$ is used. The averaging using selected data points as shown in *Fig.9* will be referred to as conditional averaging as opposed to a simple average.

Fig.9 is an example of a Cp time history which is averaged using the different average methods for a MR/TR 12° climb condition. When compared with conditional averaged Cp (*Fig. 9a*), the simple averaged Cp, using all available data points (*Fig.9b* line), still captures the MR/TR interaction behavior (as marked with arrow) but with differences in interaction peaks and phase. The MR/TR interaction behavior is totally lost in the results for a simple averaged over 1 TR revolution (Fig.9b Symbols) because the interaction seems not occur for every TR revolutions. It is obvious that the phasing is important for integer multiple

RPM. The conditional averaged aerodynamic data such as Cp and Cn will be used in following section for the presentation of test results.

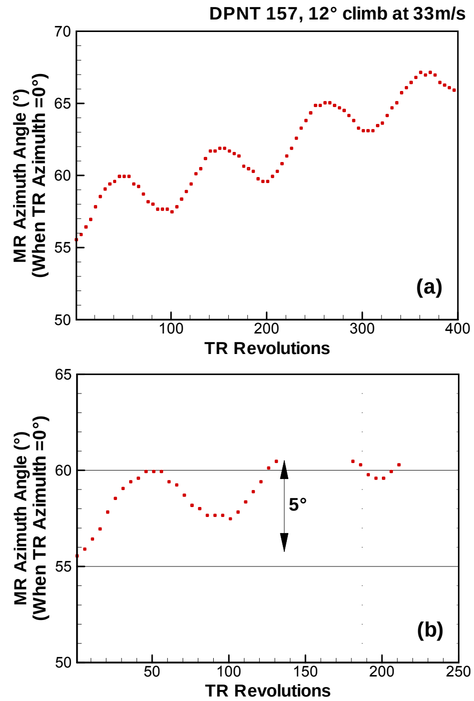

Fig.8: the MR azimuth angles as function of TR revolutions, (a) over all TR revolutions, (b) selected revolutions used for conditional averaging

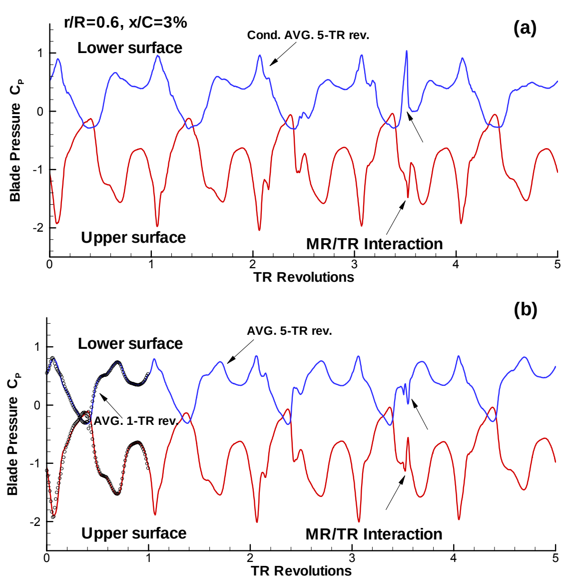

Fig.9: Cp time history over 5 TR revolutions with different average methods for a MR/TR 12° climb condition, (a) Conditional Average over 5-TR rev, (b) Simple Average over 5-TR rev and 1-TR rev.

<u>3.2 Aeroacoustic Data</u>

All acoustic data were acquired using the DNW/NLR multi-channel data-acquisition system [Ref.18]. For the inflow microphones, measurements were done in the 'step-by-step' mode with a step size of 0.5 m. Acoustic data were recorded phase-locked with the main rotor (100 revolutions, 2048 samples/revolution) and/or tail rotor (480 revolutions, 512 samples/revolution). A 10 Hz high-pass filter was used to suppress the DC component of the pressure signals. The inflow microphone signals were further processed to generate pressure-time histories, acoustic spectra, and noise contour plots using time-averaged pressure histories. As mentioned in the previous section, the simple average over one TR revolution may smooth out the behavior of MR/TR interaction. In order to avoid any wrong interpretation of acoustic results, especially when averaged results are used, the following procedures were implemented:

- The averaging was triggered with both the TR 1/5rev signal and TR 1/rev signal when the TR was the dominant noise source;
- The averaging was triggered with the MR 1/rev signal when the MR was the dominant noise source.

Conditional averaging, as explained in the previous section, was not applied to the acoustic results at this stage of the analysis. Full-scale dB(A) values were obtained by first converting the measured dB value to full-scale (frequencies divided by 2.5) and then applying A-weighting.

Acoustic data from the array microphones were synchronously measured at a fixed sample frequency of 51.2 kHz and a measurement time of 30 s. A 500 Hz high-pass filter was used to enhance the dynamic range for high frequencies. The frequency response of the individual array microphones was taken from calibration sheets. The acoustic data were processed using a block size of 4096 with a Hanning window and an overlap of 50%, yielding 750 averages and a narrowband frequency resolution of 12.5 Hz. Conventional beamforming [Ref.19] was used to obtain acoustic source plots in 1/3-octave bands. To improve the resolution and further reduce background noise from the tunnel, the main diagonal in the cross power matrix (autopowers) was discarded. The effect of sound refraction by the tunnel shear layer was corrected using a simplified Amiet method [Ref.20]. The array scan plane was placed in the main rotor plane and was rotated in accordance with the model angle of attack. The scan levels were normalized to a distance of 0.282 m [$(4\pi)^{-1/2}$], so that for a monopole source the peak level in the source plot corresponds to the Sound Power Level. The noise sources from the main and tail rotor were quantified by applying a power integration method [Ref.9] to integration contours around the main and tail rotor. Besides the conventional beamforming, a second processing method (ROtating Source Identifier- ROSI [Ref.14]) was applied to identify the noise sources on the individual main rotor blades. The scan plane was positioned in the main rotor plane and rotated along with the main rotor blades. The start position of the rotor was determined using a trigger signal that was recorded synchronously with the acoustic data. In order to limit processing time, only the first 30 revolutions after the start of each acoustic measurement were processed.

3.3 PIV Data

Data acquisition was triggered to the main rotor azimuth. Since the TR and the MR drive systems were completely independent from each other, the tail rotor blade was arbitrarily visible in the vector fields and made the analysis impossible in about a quarter of the data. A simple average of all individuals provides a good overview of the flow field and the location of the main rotor tip vortex, which was cut almost orthogonal by the set-up. For an analysis of this tip vortex a conditional average must be made, i.e. aligning all individual vortex centres first, eliminating all un-useful exposures using statistical analysis, and then averaging [Ref.21]. This eliminates the data noise but retains individual properties that got smeared out by the simple average, and also eliminates data with disturbances caused by a blade passage. A rotation into the vortex axis system was not performed, since the measurement plane was almost orthogonal to the vortex. The analysis steps are described in [Ref.22]. The post-processing of PIV data gives the global flow distribution as well as the vortex flight path.

4. Results and Discussion

The results that will be presented in the following sections concentrate on the

1. Importance and contribution of the tail rotor in relation to total noise radiation;
2. Effect of different MR and TR configuration on tail rotor noise reduction;
3. Investigation of MR and TR interaction

There are many factors which can alter TR noise radiation. These factors can be classified as consequences of the following possible interactions:

1. Interaction between the MR tip vortex and TR blade;
2. Interaction between the MR tip vortex and TR tip vortex;
3. Interaction between the MR inboard vortex and TR blade as well as TR tip vortex;
4. Interaction between the MR “wing tip vortex’ and TR blade as well as TR tip vortex;
5. Interaction between the vortex from the MR hub and fuselage, etc.

The point 1 may be reflected as extra peaks in TR acoustic and blade pressure signal. The point 2, 3 and 4 will change development of TR tip vortex so that these interactions can be observed by comparing the change of TR self BVI. The point 5 will create TR broadband noise. Therefore the data analysis will focus on correlation between acoustic data and blade pressure data.

The organization of this chapter is as follows. Section 4.1 discusses the importance of TR noise and MR/TR interaction effects. In Section 4.2 the effect of different TR noise reduction concepts will be analyzed. In Sections 4.1 and 4.2 results will be presented from the inflow microphones, blade pressures, and PIV. Results from the out-of-flow phased microphone array are discussed separately in Section 4.3.

4.1 Tail rotor noise and MR/TR interference at standard configuration

4.1.1 Acoustic results (Inflow Microphone)

For a global overview of the contribution of MR and TR to the total noise, the mean dBA value as a function of typical flight condition is given in *Fig.10*. The mean dBA value is defined here by first converting measured dBA value to full scale in frequency domain and then averaging over measured area or over all microphone positions. The comparison for two different TR rotors is also given in the plot.

In general following points can be drawn from *Fig.10*:

1. The TR is major source of noise at 12° climb and 60m/s level flight whilst the MR dominates total noise radiation during 6° descent flight in which MR BVI noise occurs;
2. The comparison of noise level for MR/TR operation with that for isolated TR show a slightly increased noise level for MR/TR operation of both NACA0012 (0.5dBA for 12° Climb) and S102 (1.1dBA for 12° Climb);
3. The mean noise level is slight higher for TR with S102 profile.

Point 2 may be considered as effect of MR/TR interaction. Because the thrust requirement of the TR depends strongly on flight condition, the higher TR thrust values for climb and level flight condition contribute to the higher TR noise. The small increment of TR noise level in MR/TR combined condition seems to indicate the effect of the MR wake on the TR noise may be secondary.

The influence of MR/TR on TR noise can be demonstrated more in detail by observing noise contour plots because the noise contours can provide not only an overall estimation of the noise levels, but also the noise directivity. The full scale dBA contours over measured area are given in *Fig.11 (a, b and c)*. The location of the MR disc and TR rotation plane are indicated by the circle and thick line respectively.

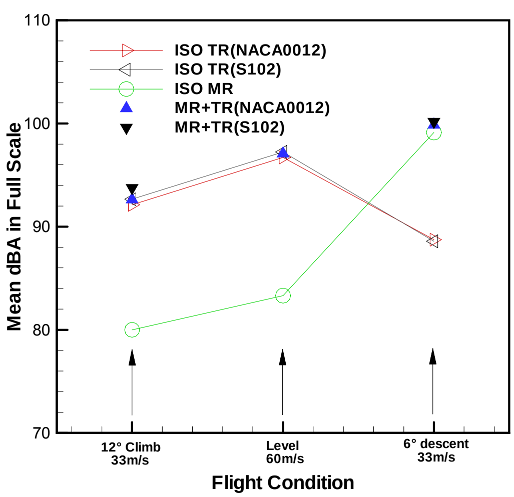

Fig.10: Mean dBA value as a function of typical flight condition and MR/TR configurations

The results show that the maximum noise area for 12° climb case for isolated TR equipped with either NACA0012 (*Fig.11b* left) or S102 blade (*Fig.11a* left) is located at just upstream of the TR and around TR rotational plane where TR thickness noise dominates. The obviously increasing loading noise contributions in 60m/s level flight in TR thrust- and outflow-direction are observed as shown in *Fig.11c* left. Although the thickness noise still plays an important role in overall noise level. The comparison of isolated TR shown in *Fig.11a* and *Fig.11b* indicates the maximum noise level located at TR rotational plane for S102 TR is almost 2dBA less than that of NACA0012 TR. This is due to the lower thickness of the S102 TR blade. The MR noise is less important in both climb and level flight, as shown in *Fig.11a* (middle) to *11c* (middle). Increased MR level upstream of MR in level flight due to increased local tip Mach number is observed as shown in *Fig.11c* (middle). There is a noticeable increase in the background noise for the microphone positions which are located downstream of vertical sting support of rotor test stand. The increased background noise as shown in *Fig.11c* (middle) around TR is due to interaction of microphone and vortices shed from support system. But the magnitude of the background is till several dB lower than real physical signal and can be neglected in noise evaluation.

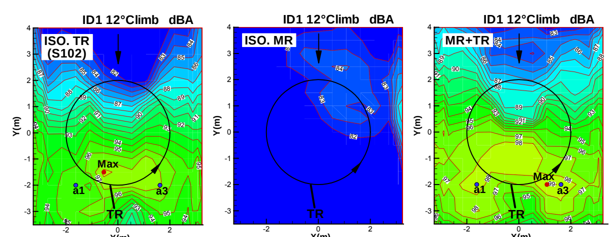

(a) 12º Climb at 33m/s, TR equipped with S102

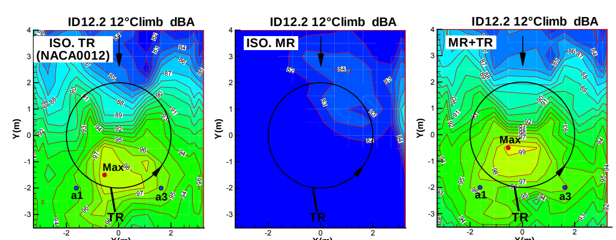

(b) 12º Climb at 33m/s, TR equipped with NACA0012

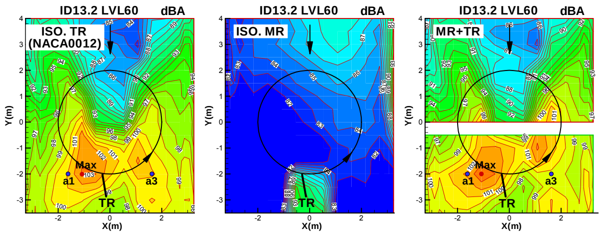

(c) 60m/s Level flight, TR equipped with NACA0012

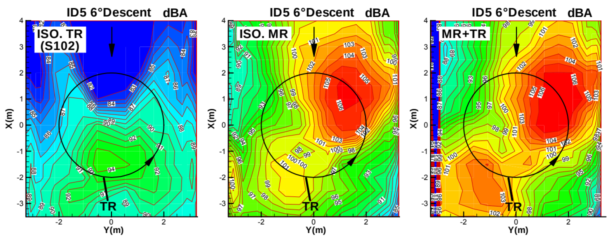

(d) 6º descent flight at 33m/s, TR equipped with S102

Fig.11: Comparison of full scale dBA contours for isolated TR, isolated MR and the combined operation of both MR and TR in different flight conditions

In MR+TR(S102) cases, in low speed 12° climb condition, the maximum noise position (marked with red point) in *Fig.11a* (left) for isolated TR has moved to the right side of TR in *Fig.11a* (right) for MR+TR. This is because of the increasing loading noise due to MR/TR interaction. At same flight condition, the slightly increasing loading noise is observer for TR equipped with NACA0012 blade in *Fig.11b* (right), but the maximum noise position still located about TR rotational plane, which indicates that TR thickness noise is the dominant noise source. The increased loading noise levels for 60m/s level flight are also observed in TR thrust- and outflow-direction for level flights, as shown in *Fig.11c* (right).

There is obviously a shadow area (V form in contour plots upstream of TR) especially for TR noise which is due to the scattering effect of the fuselage.

The acoustic pressure time histories can provide detailed information to judge the noise aspect of each test case. In order to identify possible interference of MR wake on TR noise, *Fig.12* gives the comparison of averaged time history for isolated TR and for the combined operation of MR and TR on the microphone positions marked as (a1, a3) in *Fig.11* towards the rear of the MR disc. The plots cover 5 TR revolutions. The corresponding power spectrum from this time history is given in *Fig 13*. It is interesting to notice that most of the BVI like pressure spikes that occurred in isolated TR condition also occurred in MR/TR combined cases for all the flight conditions studied here, although some peaks have slightly intensity differences. Therefore, these pressure spikes can't be related to MR tip vortex/TR blade interactions. It appears to be the results of TR self generated BVI. In addition, the BVI peaks almost repeat themselves revolution by revolution for isolated TR condition. This repetition still persists for combined MR+TR cases but with clear variations in the magnitude from TR revolution to revolution. This is because the local inflow encountered by TR varied with revolutions, which is determined by the RPM ratio of MR and TR. This behavior is also observed in blade pressure time history described in following section. It is obvious that the magnitude of the BVI peaks is higher in combined MR+TR cases, which contributes to higher sound pressure level in lower and mid-frequency ranges as shown in all spectrum plots in *Fig.13*. *Fig.13* indicates the increasing spectrum levels in mid frequency range for isolated TR cases when comparing with MR+TR case, although generally in high frequency the spectrum level is lower.

In order to see more clearly how interaction of MR wake on TR effects the radiated noise, a zoom view on *Fig.12a* (left) for 12° climb case is given in *Fig 14*. In addition, a source tracing procedure is applied in order to correlate received acoustic signal with blade position when noise is generated. The vertical tracing line is given for blade spanwise position at r/R=0.7. The azimuth position ψ relates to the blade being considered here namely the TR blade. The small wiggle occurring between $\psi = 160^o$ and $\psi = 180^o$ on the curve of MR+TR case is believed to be caused by MR tip vortex and TR interactions, because the MR tip vortex cut by the TR blade is observed within the azimuth angle range in both the blade pressure and PIV data described in following sections. The small "hill" between $\psi = 130^o$ and $\psi = 160^o$ where the fin is located can be explained as the effect of the fin.

The use of a low pass digital filtering can help investigate the cause of the increasing spectrum levels from 3000Hz to 4000Hz for isolated TR cases as shown in *Fig.13a* (left), for example.

After using a digital filtering to filter out signal higher than 3000Hz, it is found that the peaks pointed by arrows in Fig. 14 is the cause of higher spectrum level in this frequency range. Since the sound pressure level within this frequency range is relative lower than that below this frequency range, the effect on overall level is quite small.

From acoustic test result analysis (inflow microphone), it can be stated that

1. MR/TR interaction has slightly increased the TR mean dBA level for both climb and level flight conditions;
2. TR self BVI noise may be the main source of noise and the level of extra BVI peaks due to interaction of MR tip vortex and TR blade is quite small;
3. Interactions of TR with the mean flow disturbances caused by the MR and fuselage may be more important than individual interaction of TR with MR tip vortex;
4. MR wake can disturb TR inflow and therefore reduce TR high frequency noise in MR+TR cases.

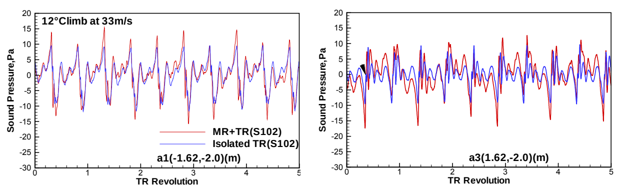

(a) 12º Climb at 33m/s, TR equipped with S102

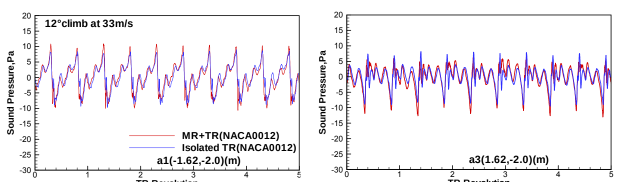

(b) 12º Climb at 33m/s, TR equipped with NACA0012

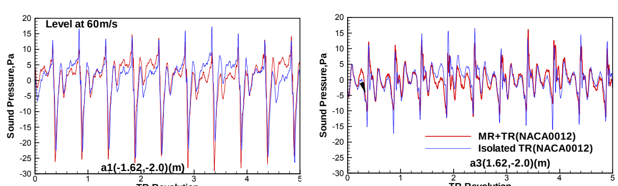

(c) 60m/s Level flight, TR equipped with NACA0012

Fig.12: the comparison of averaged time history for isolated TR and for the combined operation of MR and TR on the microphone positions marked as (a1, a3) in Fig.11.

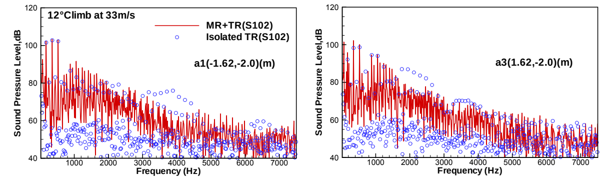

a) 12º Climb at 33m/s, TR equipped with S102

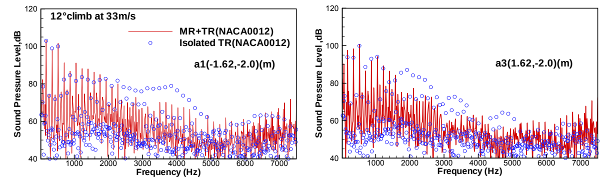

(b) 12º Climb at 33m/s, TR equipped with NACA0012

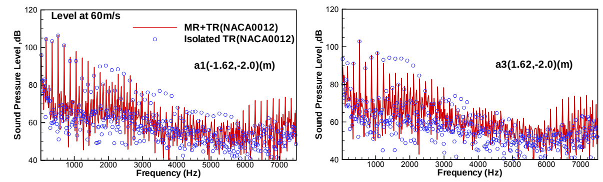

(c) 60m/s Level flight, TR equipped with NACA0012

Fig.13: the comparison of acoustic spectrum for isolated TR and for the combined operation of MR and TR on the microphone positions marked as (a1, a3) in Fig.11.

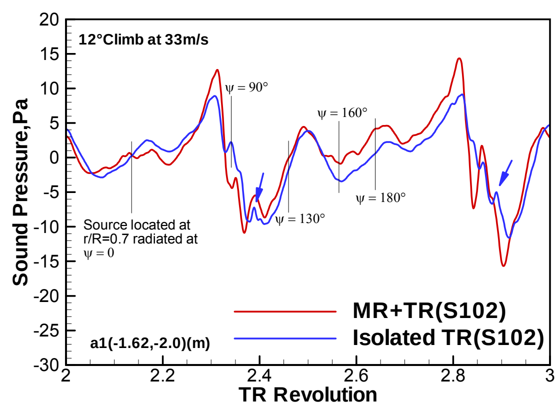

Fig.14: a zoom view on Fig.12a (left) for 12° climb case together with source position (vertical line)

4.1.2 Aerodynamic results

Blade Pressure

The blade sectional loads and blade pressure at leading edge sensors can be used to detect the presence of MR interaction effect on TR aerodynamics which may be the source of TR radiated noise. The pressure data post processing is described in previous section and will be used here. Both the averaged blade pressure and sectional loads are explored for different flight conditions in which TR noise is the dominant noise source. It is useful to investigate the TR blade pressure time histories, especially for the sensors close to blade leading edge, in order to correlate them with noise radiation characteristics.

Fig.15 gives conditional averaged TR blade pressure time histories for the 12° climb case as a function of TR revolutions. TR upper and lower side blade pressure near the leading edge at 3% chord and different spanwise locations are compared for the isolated TR (S102) and combined operation of MR+TR (S102).

The blade pressure time histories for both isolated TR and MR/TR combined conditions show that on the advancing blade side there are strong Cp peaks on both upper surface (negative) and lower surface (positive). The peaks occur for all TR revolutions. Since the peaks occur for both isolated TR and MR/TR cases, the peaks are caused by the interaction of TR blade trailing tip vortex and the preceding TR blade. The localized increase in Cp is due to the velocity induced by the vortex opposing blade rotation and almost parallel to the blade axis. These peaks contribute to acoustic level in lower and middle frequency range as shown in *Fig.13*. The effect of the fin on Cp occurres at around 130° to 160° azimuth angle and seems to be stronger for MR/TR combined conditions.

There are loading peaks during the 4th TR revolution as indicated by arrows for all spanwise positions given in *Fig.15* (left), but these peaks do not occur in isolated TR cases in *Fig.15* (right). It is believed that the occurrence of peaks is caused by the interaction of a MR blade tip vortex and TR blade. A local increase in Cp value is observed for sections other than r/R=0.7. *Fig.20* demonstrates the track of MR tip vortex flight path determined from the positions of interaction peaks on pressure time histories together with those obtained from flow field measurement (PIV). The results are correlated with PIV data. The circles in the plot represent different radial position on the TR. Because the strongest interaction occurs in the inner part of the blade in which the speed is lower, there is less contribution to the noise, as was explained in previous section.

Fig.16 illustrates a similar comparison for the 60m/s level flight, but the interaction peaks caused by interaction of MR tip vortex and TR blade are not as strong as in climb case.

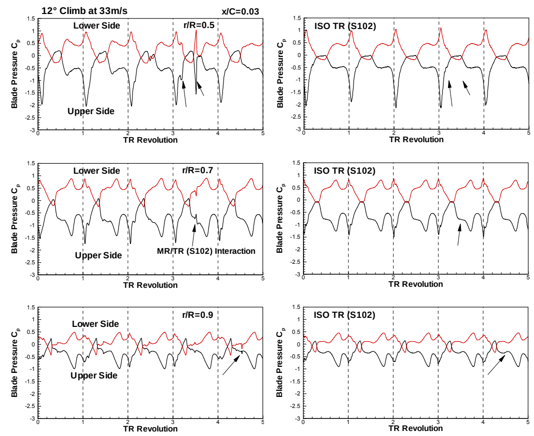

Fig.15: the comparison of leading edge blade pressure time history as function of TR revolutions for isolated TR and for the combined operation of MR and TR, 12° climb case at 33m/s. Left: MR+TR, Right: Isolated TR

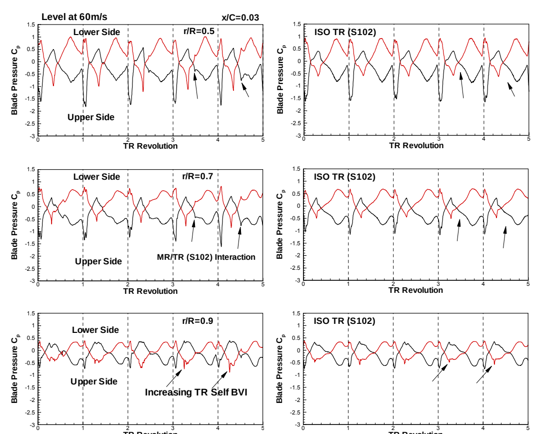

Fig.16: the comparison of leading edge blade pressure time history as function of TR revolutions for isolated TR and for the combined operation of MR and TR, level flight case at 60m/s. Left: MR+TR, Right: Isolated TR

From TR blade pressure data analysis, it can be stated that

1. The interactions of MR tip vortex and TR blade are observed for both climb and level flight conditions.
2. Correlation with acoustic results shows that their overall effect on tail rotor noise is small.

3. Individual interaction of TR with MR tip vortex may have secondary effect on noise.

Flow Field - PIV results

An overview of the simple average flow field of plane 1 (between the tail rotor and the fin) and plane 2 (blowing side of the tail rotor), with the mean velocities subtracted, is given in *Fig.17*. The main rotor tip vortex enters in the middle of the left side and is convected downstream and downwards to the right. Reflections from the fin (bottom left to the centre) are much less in plane 2 due to the larger distance. The main rotor tip vortex is visible at (x, z) = (65,56) for Ψ_{MR} = 30° and (90,49) for Ψ_{MR} = 120°. Reflections from the fin indicate its position in the figure (bottom left to the centre). The tail rotor disk is indicated by the large circle.

The high speed forward flight case is shown in Fig.18. Only three of the 5 observation areas were covered here. Again, the fin is reflecting in the middle, and in plane 1 the drag of the tail rotor shaft is dominating the right half of the figure. Reflection effects are significantly reduced in plane 2. Reflections from the fin indicate its position in the figure (centre). The main rotor tip vortex is visible at (x, z) = (93, 60) for Ψ_{MR} = 30°.

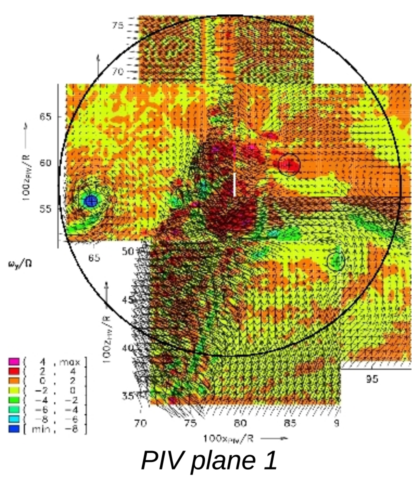

PIV plane 1

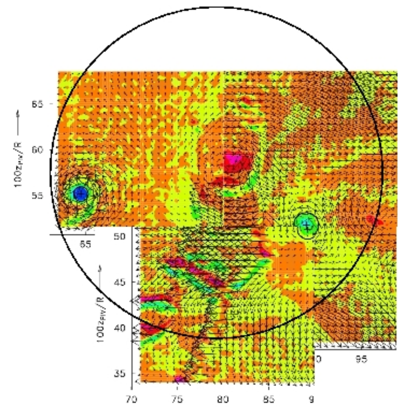

PIV plane 2

Fig.17: Flow field and vorticity distribution in plane 1 (left, y/R = -0.032) and in plane 2 (right, y/R = -0.112), V = 33 m/s, 12° climb.

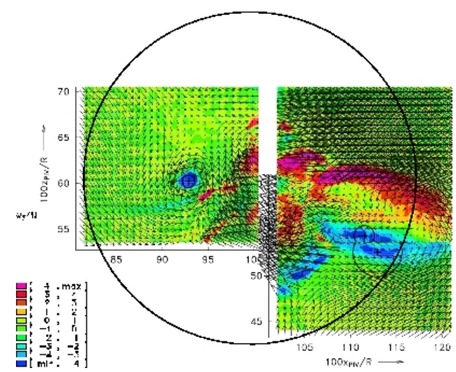

PIV plane 1

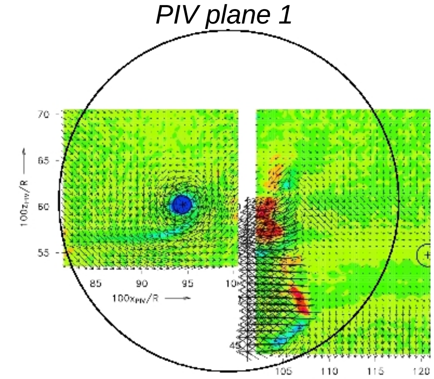

PIV plane 2

Fig.18: Flow field and vorticity distribution in plane 1 (left, y/R = -0.032) and in plane 2 (right, y/R = -0.112), V = 60 m/s, level flight.

Fig.19 shows two instantaneous flow field and vorticity distributions taken from the sequence PIV data in window 1 of plane 1 for low speed 12° climb case at Ψ_{MR} = 150°. The double vortex core rotating in same direction is observed (Fig.19b).

The position of the TR blade marked as red line is also visible in the window. Close examination of flow field especially with the data animation has revealed a MR tip vortex splitting due to the TR blade cutting through it.

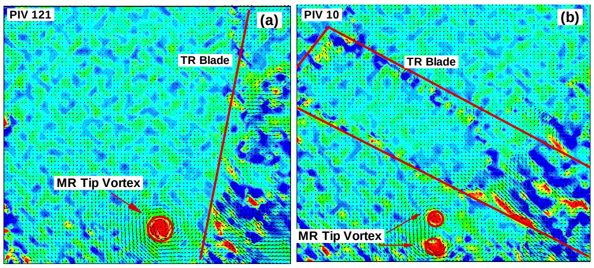

Fig.19: two instantaneous flow field and vorticity distribution in window 1 of plane 1 for low speed 12° climb case at Ψ_{MR} = 150°.

In Fig.20 the vortex flight path through the PIV planes is given in TR hub coordinates. The time increment between the symbols is 30° of MR azimuth. The vortex is clearly visible at (MR = 30° in both flight conditions, and also for (MR = 60° at V = 33m/s. These positions are ahead of the area affected by fin and TR hub reflections.

In plane 1, the vortices of the high speed case closely pass the TR hub and are difficult to detect thereafter, see Fig.18. The disturbances were not that severe in the low speed climb condition where the vortices pass below the TR hub. Some differences in convection become visible downstream of the tail rotor hub. At low speed climb the convection in plane 1 is larger than in plane 2, which can be explained by the suction and associated acceleration on this side of the TR disk. The opposite is true in high speed level flight. In this case the presence of the TR shaft appears to decelerate the flow. In any case the vertical position becomes different after passage of half the tail rotor disk area. The track of MR tip vortex flight path determined from the positions of interaction peaks on pressure time histories is marked as solid circle in the figure. The circles in the plot represent different radial position of TR.

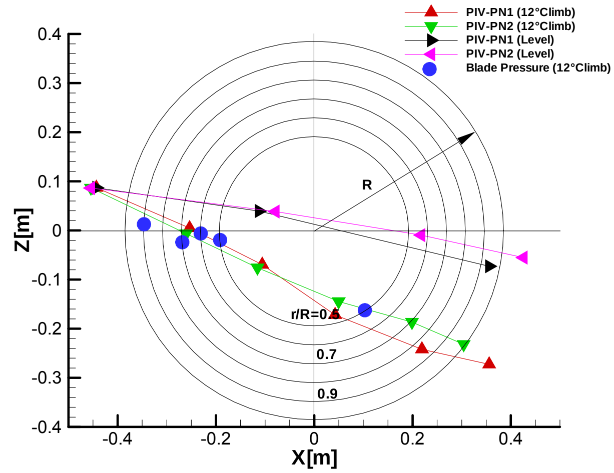

Fig.20: Main rotor vortex flight path through the tail rotor disk at V=33m/s, 12° climb as well as the track of MR tip vortex flight path from pressure time histories (solid circle points)

4.2 Tail rotor noise reduction potential

An important aspect of the EU HeliNOVI project is to assess the acoustic benefit in view of realistic helicopter operation and to eventually establish design guidelines for future less noisy helicopters with conventional tail rotors. Presented in the following sections is an assessment of the TR noise reduction potential through variation of blade and tip speed, through change of the TR sense of rotation, and by modification of the TR position.

4.2.1 Change TR rotational direction

Previous TR noise research found that it is desirable for TR to rotate Advancing Side Down (ASD) to minimize the interactions with ground and “wingtip” vortices as well as TR noise. The original BO105 TR is rotated in Advancing Side Down direction. In order to verify whether this preferable TR rotational direction is a general rule for TR noise reduction, the test is conducted by changing TR rotational direction from ASD to Advancing Side Up (ASU). The TR with a NACA0012 profile is used in this test.

Aeroacoustic and aerodynamic results

As a global overview of the noise radiation, the mean dBA value as a function of 3 different flight conditions is given in *Fig.21* for two different TR rotational directions; ASD & ASU. When compared to TR in ASD mode, a noise reduction of more than 5 dBA is observed for the 12° climb and 60m/s level flight conditions in ASU mode. There is no change on overall noise radiation for 6° descent while MR BVI noise is the dominant noise source. In order to verify whether this noise reduction is caused by changing TR performance, the TR thrust, TR power and helicopter vertical force as function of different flight condition and rotational mode (ASD & ASU mode) is given in *Fig. 22*. The variations in TR performance for TR in ASD & ASU modes are negligible.

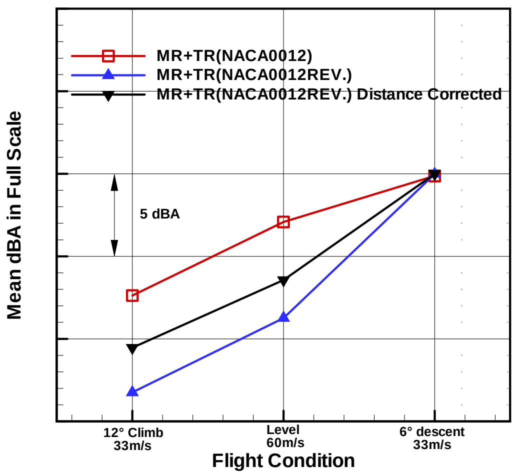

Fig. 21: Mean dBA value as a function of typical flight condition for TR in ASD & ASU mode

It is obvious that one factor in the TR noise reduction is the increased distance from the source located in advancing blade to the observers (microphones) when TR is rotating in ASU mode. The maximum noise reduction due to increasing the advancing blade distance can be estimated as 2.7dB for 12° climb and 2.3 dB for level flight by assuming a source localized at 80% radial position of TR. By making a distance correction to the noise reduction with above mentioned maximum value, a conservative noise reduction due to change of TR aerodynamic behavior can be estimated (marked as distance corrected value in *Fig.21*). There is no change for 6° descent because the MR BVI noise dominates. The results of noise reduction by reversing TR from ASD to ASU mode contradicts the finding (Westland Lynx) of the previous TR noise research.

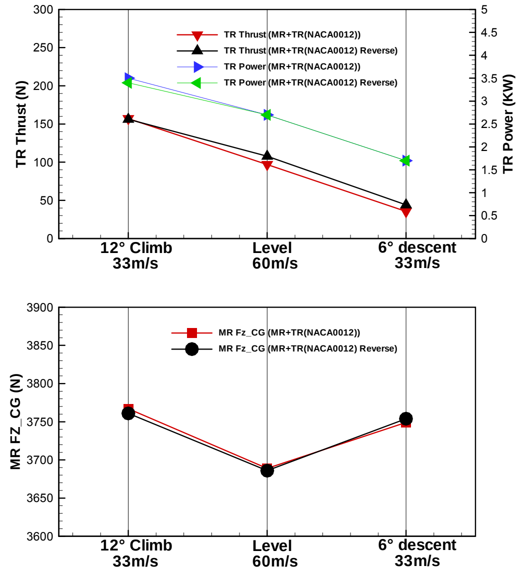

Fig.22: the TR thrust, TR power and helicopter vertical force as function of different flight condition and rotational mode

The influence of the direction of TR rotation on TR noise can also be demonstrated more in detail by observing noise contour plots as shown in *Fig.23* for two different flight conditions at 12° climb and 60m/s level flight. The comparisons show a noise reduction, at the maximum noise area marked, is about 8 dBA for the 12° climb case (Fig.23a) and about 6dBA for 60m/s level flight condition (Fig.23b). The contour plots show the maximum noise area in ASU TR mode has shifted upstream. The shifting is due to possible higher source position in ASU TR mode. The comparison of the spectrum at the maximum noise position, marked as red point or Max in *Fig.23*, indicates the reduction of not only thickness noise (lower frequency range) but also loading noise, especially self BVI noise (mid-frequency range), as shown in *Fig.24*.

Analyzing the blade pressure data, *Fig.25* and *Fig.26* give conditional averaged TR blade pressure time histories at 3% chord and different spanwise locations for both the 33m/s 12° climb case and 60m/s level flight respectively. The blade pressure time histories show a dramatic reduction of Cp peaks on the advancing blade side (such as for the azimuth position marked with arrows) for both upper and the lower surface in TR ASU mode. These peaks contribute to the sound pressure components in lower and mid frequency range. The reduction in these Cp peaks is beneficial for the noise reduction.

From above analysis it can be stated that the TR noise reduction by reversing TR rotational direction from ASD to ASU has benefit from

1. Increasing noise source to observer distance;
2. Shifting TR advancing blade away from the MR wake including tip vortex;
3. Advancing side blade away from tail fin;
4. Changing fuselage scattering effect

Points 2 and 3 result in a weak self TR BVI and therefore introduce less noise.

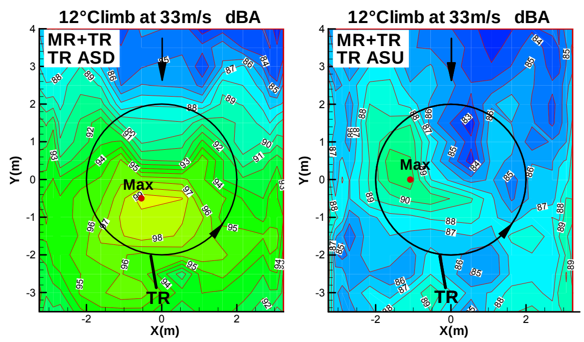

(a) 12º Climb at 33m/s, TR equipped with NACA0012

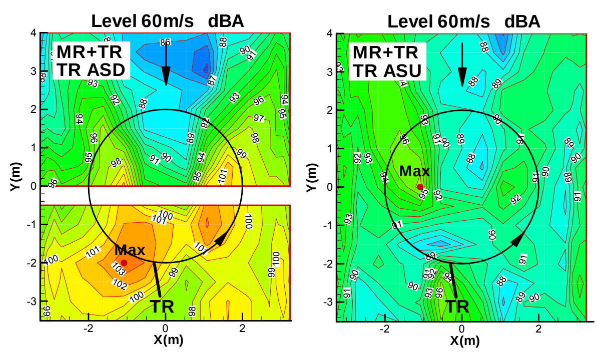

(c) 60m/s Level flight, TR equipped with NACA0012

Fig.23: Comparison of full scale dBA contours for the combined operation of both MR and TR in different flight conditions and TR rotational direction

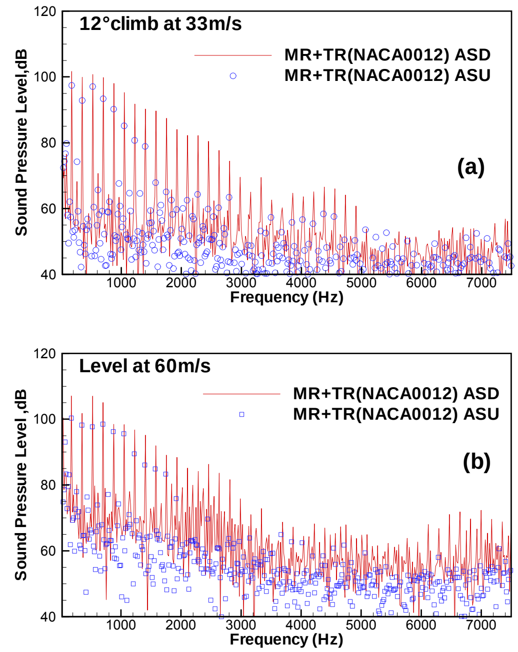

Fig.24: The comparison of the spectrum at maximum noise position marked as red point or Max in Fig.23

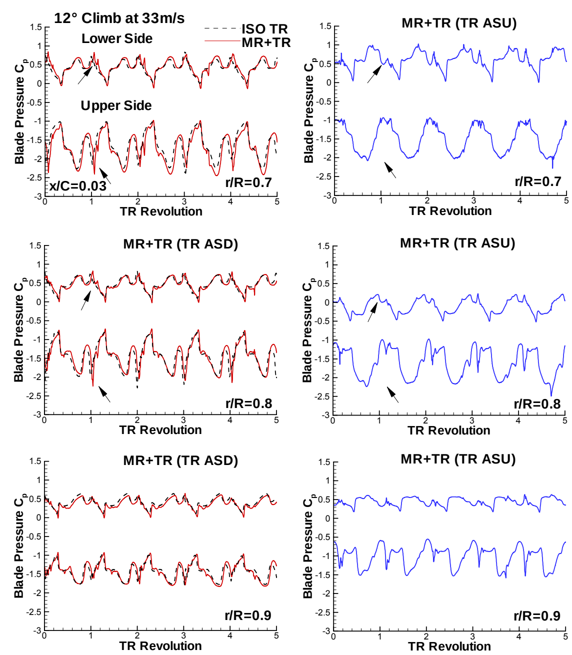

Fig.25: the comparison of leading edge blade pressure time history as function of TR revolutions for the combined operation of MR and TR in different TR rotational mode, 12º climb at 33m/s. Left: TR ASD, Right: TR ASU

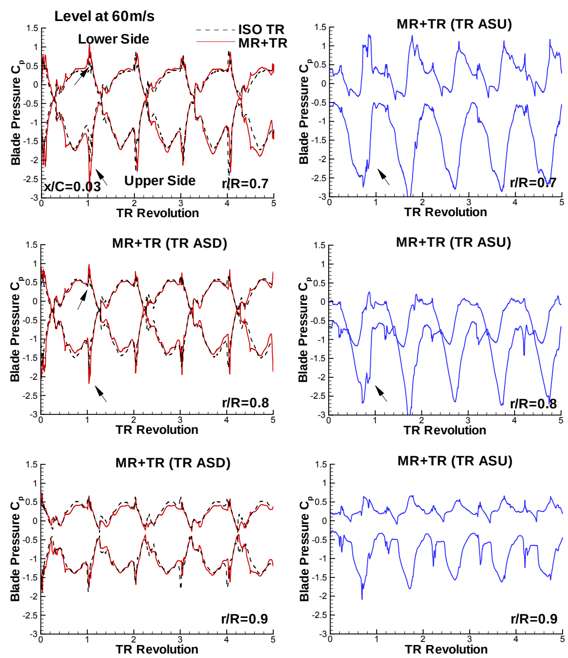

Fig.26: the comparison of leading edge blade pressure time history as function of TR revolutions for the combined operation of MR and TR in different TR rotational mode, 60m/s level flight case at 60m/s. Left: TR ASD, Right: TR ASU

4.2.2 Change TR Position

The TR location relative to the MR and helicopter operating conditions are two major factors that determine the vortex trajectories on the TR disk. The potential noise benefit resulting from a change in TR offset in the vertical direction position (to minimize or avoid the interaction with the main rotor wake) will be quantified. *Fig.27* illustrates new TR position with respect to original TR position. The TR is equipped with S102 profile in this test.

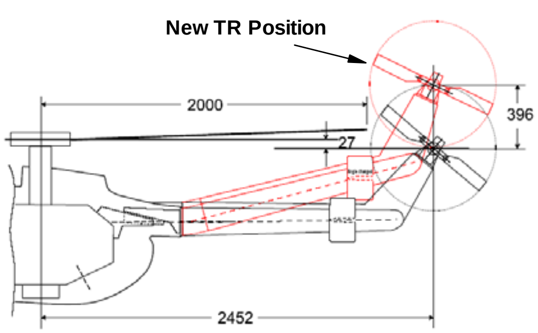

Fig.27: Drawing of new TR position with respect to original TR position

Aeroacoustic and aerodynamic results

Fig. 28 gives the mean dBA value as a function of 3 different flight conditions for new TR position and compares with that for the original TR position. As discussed previously, a conservative noise reduction due to change of TR aerodynamic behavior can be estimated by adding back the maximum noise reduction due to increasing the advancing blade distance as show in *Fig.27*. The results demonstrate that the noise reduction for new TR position is mainly due to increasing the advancing blade distance rather than changing TR aerodynamic behavior.

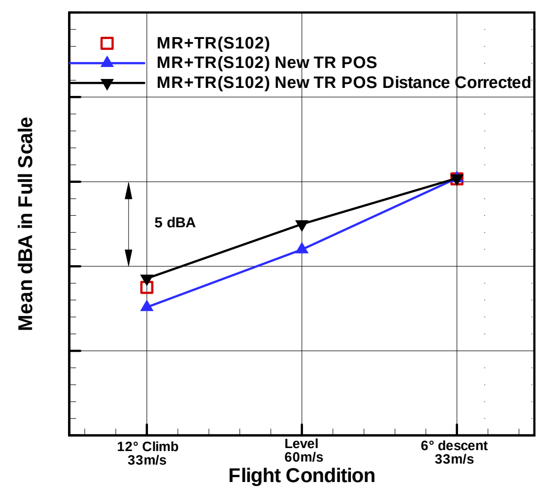

Fig.28: Mean dBA value as a function of typical flight condition for TR in original and new position

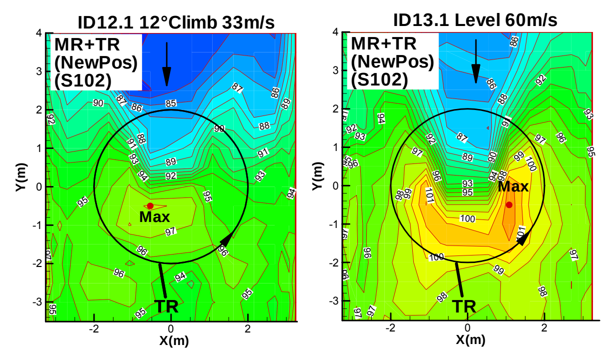

Fig.29: noise contours over measured area for 12° climb-and 60m/s level- flight condition at new TR position

The noise contours over the measured area are given in *Fig.29* for 12° climb and 60m/s level flight conditions. When comparing with the results from normal BO105 TR position as shown in *Fig.23* for

12° climb condition, the contour plots show a slight shift of the maximum noise area in the upstream direction due to the high source position of TR advancing side. The decreasing of thickness and loading noise level is observed. By looking at the comparison of blade pressure data with that at normal TR position for this flight condition as shown in *Fig.30,* we find that no TR blade and MR tip vortex interaction peaks (pointed with arrow) is observed in new TR position case. The two time histories indicate quite similar behavior especially for advancing side peaks. There is no direct comparison that can be made for noise contour in 60m/s level flight, but comparison of blade pressure data with that at normal TR position, as shown in *Fig.31*, demonstrates the reduction of advancing side Cp peaks for the TR in new TR position case. The reduction of TR loading noise is then expected.

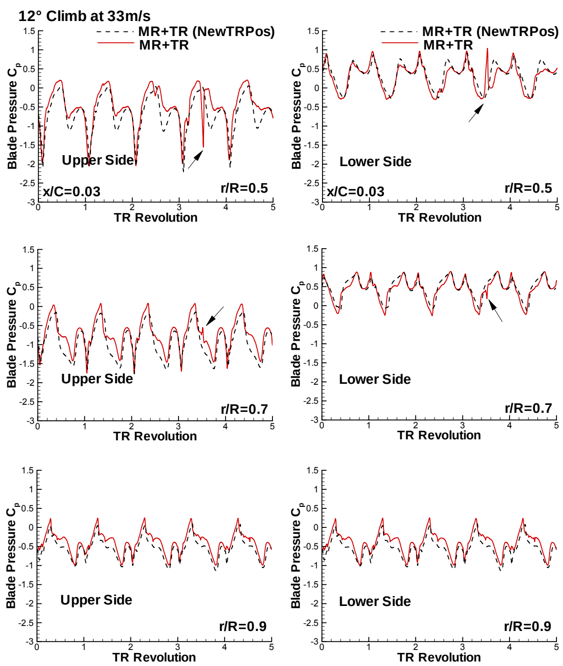

Fig.30: the comparison of leading edge blade pressure time history as function of TR revolutions for the combined operation of MR and TR in different TR position, 12º climb at 33m/s. Left: Upper side, Right: Lower Side

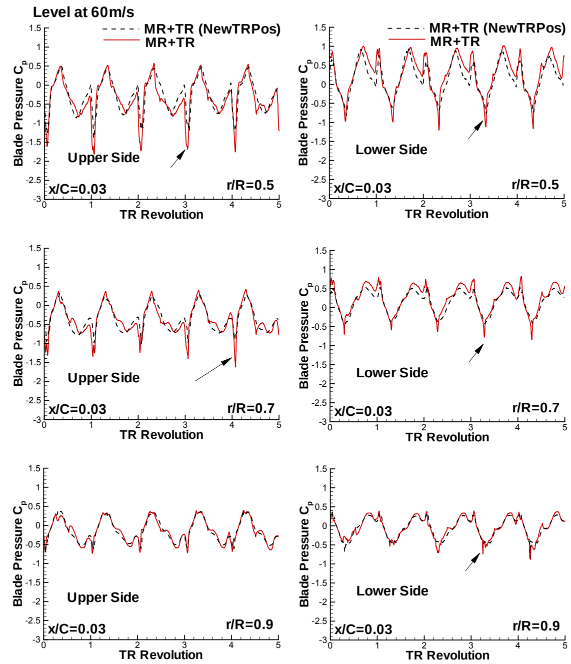

Fig.31: the comparison of leading edge blade pressure time history as function of TR revolutions for the combined operation of MR and TR in different TR position, Level flight at 60m/s. Left: Upper side, Right: Lower Side

4.2.3 Lower tip speeds

It is well known that the overall sound level is related to tip speed. A certain noise reduction was expected to occur due to the reduced blade tip speed of MR and TR. The tip speed reduction of about 10% for both MR and TR was tested. The rotors were trimmed in order to keep the same thrust as that of nominal tip speed. The thrust reduction resulting from a reduced tip velocity was compensated by an increasing blade collective pitch.

Aeroacoustic results

The aeroacoustic results are shown in *Fig.32* and *Fig.33*. *Fig.32* indicates that the rotors are indeed in general quieter than with the original tip speed. As results of TR tip speed reduction, the beneficial effect on reduction of thickness noise is clearly observed for 12° climb flight condition. In this flight condition the maximum noise area is shifted from thickness noise dominant area (TR rotational plane) as shown in *Fig.23* or *Fig.11a* to loading noise dominant area given in *Fig.33*. The reduction of MR BVI noise especially in the retreating side area is obvious by comparing *Fig.33* and *Fig. 11d*. Therefore it is concluded that reducing tip speed is most effect way to reducing noise.

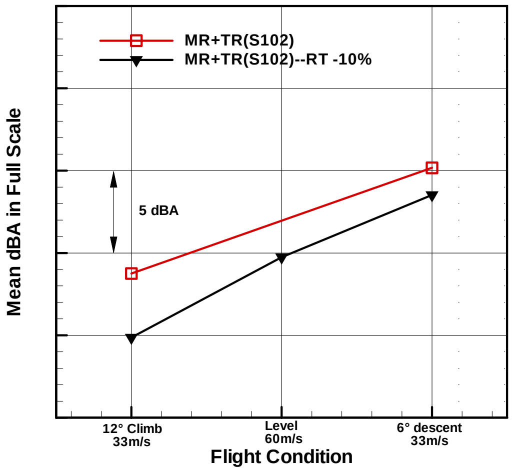

Fig. 32: Mean dBA value as a function of typical flight condition, Effect of tip speed reduction

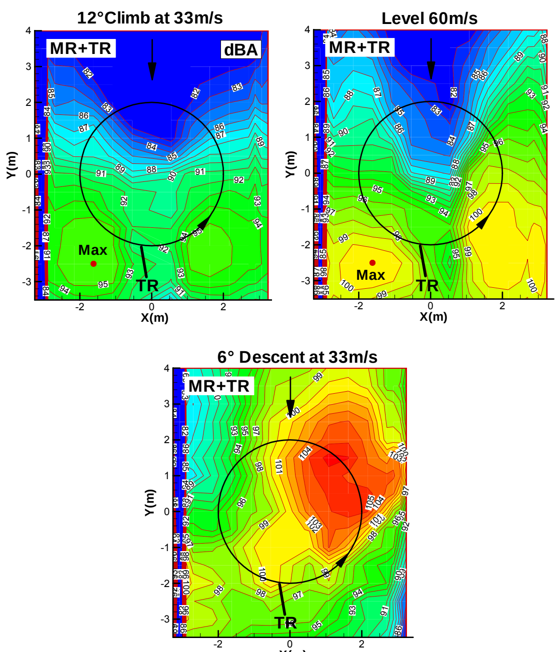

Fig.33: Noise contour plots at three typical flight condition, Effect of tip speed reduction

4.3 Phased array results

In this section selected results will be presented to illustrate the capabilities of the phased array technique for helicopter noise. In order to explain the difference between the inflow contour plots and the so-called acoustic 'source plots' from the phased array, Fig.34 shows a picture of the test set-up with the out-of-flow microphone array, the inflow scan plane, and the array scan plane. Whereas the inflow contour plots show the overall noise radiation (from all sources) in different directions, the phased array identifies the different sources for a fixed observer position (i.e. the array position). Thus, both methods provide complementary information on the location and directivity of the noise sources. The relation between inflow contour plots and acoustic source plots will be further elucidated in the next sections. Unless explicitly mentioned otherwise, the results in this section are for the MR+TR configuration. In the array processing random averaging was applied (i.e. not synchronised to MR or TR revolutions), so that both main and tail rotor noise sources will show up in the source plots (if present). This enables an assessment of the relative importance of both sources. Synchronised averaging was also applied to produce acoustic source plots of MR or TR noise only, but these results will not be presented here. In Section 4.3.1 results are discussed for the descent condition, where MR noise is dominant. Section 4.3.2 presents results for a case where TR noise is dominant (high speed level flight). The results are presented in 1/3-octave bands (linear dB) at model scale frequencies. Unless explicitly mentioned otherwise, results are shown for the array position below the model.

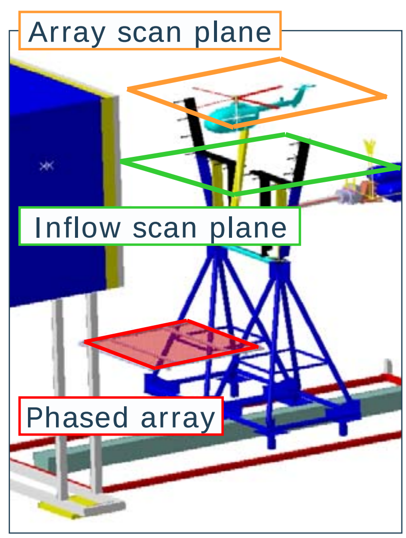

Fig.34: Test set-up with phased array and different scan planes

4.3.1 Main rotor noise

Fig.35 shows acoustic source plots (2kHz) for both array positions in the descent case. As a reference the pressure history (high pass filtered) for a transducer on the outer blade is shown as well (zero azimuth is when the blade points downstream). The source plots clearly show that MR noise is dominant over TR noise. Furthermore, for the upstream array position the advancing side is dominant, while for the array position below the model the retreating side is dominant. The azimuth angles for the dominant source positions are about 60° and 310°, which is consistent with the BVI positions in the blade pressure history. The range of the color scale for the source plots is 12 dB, but it should be noted that the maximum in the upstream source plot is 8 dB higher than the maximum for the 'below model' plot. Since the source levels are normalized to a constant distance, this means that the advancing side source is 8 dB louder than the source on the retreating side (for the present radiation directions).

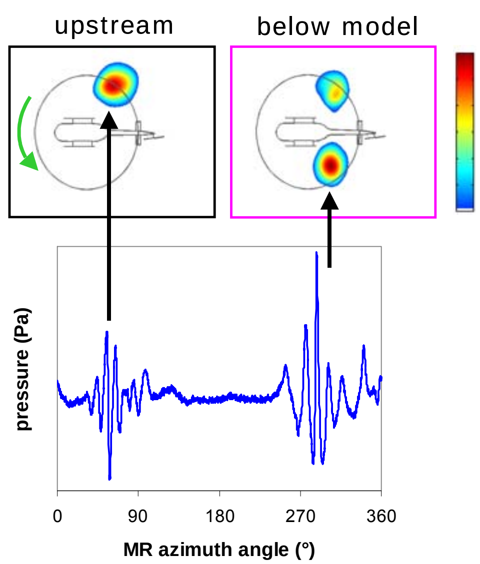

Fig.35: Acoustic source plots and blade pressures showing BVI noise source locations for the descent condition. The source plots (2 kHz) show the noise sources in the rotor plane for both array positions (upstream and below the model.

More insight in the radiation characteristics of the BVI noise can be obtained by comparing the source plots to the inflow contour plot at the same frequency (*Fig.36*). The range of the color scale is again 12 dB. In order to allow a good comparison, the projection of the phased array surface on the inflow scan plane (as 'seen' from the dominant source locations in *Fig.35*) is plotted for both array positions (see also *Fig.34*). In *Fig.36* it can be seen that the major red spot is due to the advancing side source, whereas the green source area more downstream is due to the source on the retreating side. The level difference between these two source regions is consistent with the difference between the maxima in the source plots of 8 dB. Thus, the array provides additional information about the source locations and directivity that cannot be extracted from the inflow contour plots alone. In the remainder of this paper, results will be shown only for the array position below the model.

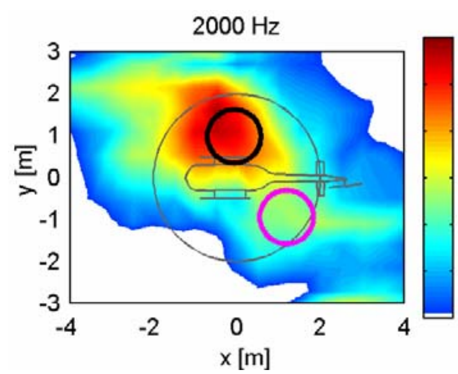

Fig.36: Inflow contour plot for the descent condition. The projection of the phased array surface on the inflow plane is indicated by the black and pink circles (for both array positions, compare to Fig. 35)

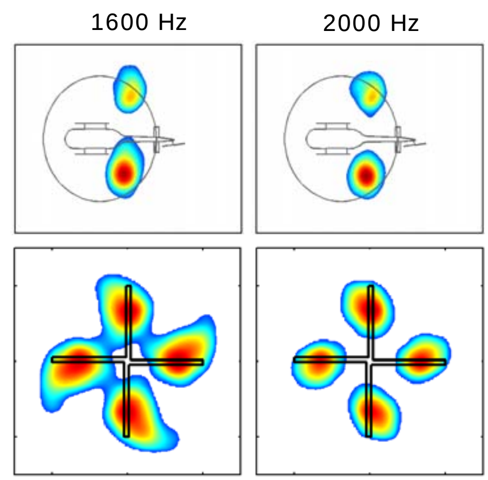

Fig.37: Standard acoustic source plots (upper row) and corresponding ROSI plots (lower row) for the descent condition

In order to compare the noise sources for the different main rotor blades, a second processing method was applied to the array results (ROSI-Rotating Source Identifier, Ref.15). *Fig.37* shows

ROSI plots for the descent configuration together with the corresponding standard source plots. The ROSI plots show the source locations on the individual blades, averaged over 30 revolutions. Since these plots show the integrated noise production over all azimuthal angles, the orientation of the plot is arbitrary. It can be seen that there are only small differences in the BVI noise production of the different blades. Although ROSI was previously mainly used to identify broadband self-noise from rotor blades, [Ref.11,12, and 15], these results illustrate that ROSI can also be applied to impulsive noise. In the next section it will be shown that ROSI can even provide information on tail rotor noise.

4.3.2 Tail rotor noise

Although results were analysed for all flight conditions, for conciseness this section will focus on the high-speed level flight condition (60 m/s) with the S102 tail rotor. *Fig.38* shows two acoustic source plots which illustrate that the relative importance of main and tail rotor noise depends on frequency. This is also obvious from the integrated spectra in the same figure, which confirm that for the low frequencies tail rotor noise is dominant and for the high frequencies main rotor noise. As shown in *Fig.10* and *11* of inflow microphone analysis, in terms of overall A-weighted sound levels, the tail rotor is clearly dominant.

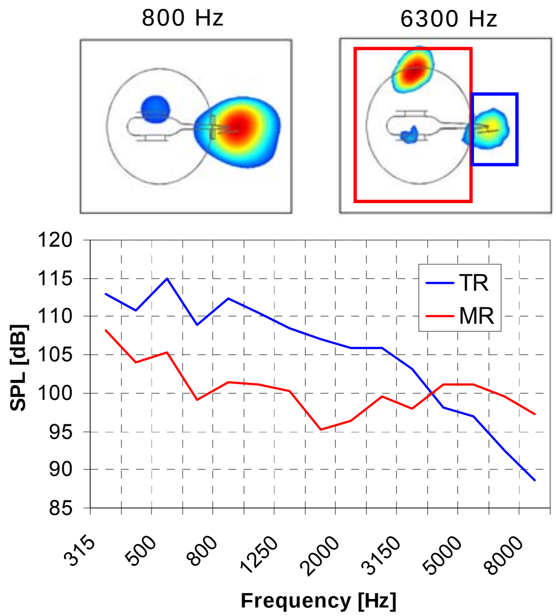

Fig.38: Acoustic source plots and integrated spectra for level flight (60 m/s). The integration contours for main and tail rotor are indicated in the 6.3 kHz source plot

Using the power integration method, the effect of the different tail rotor noise reduction concepts was assessed as a function of frequency (*Fig.39*). The tail rotor integration contour was the same as in *Fig.38*. It can be seen that reversal of tail rotor sense of rotation (from 'advancing side down' to 'advancing side up') gives a significant broadband noise reduction. This reduction is consistent with the results from the inflow noise contours (*Fig.21* and *23*). Note that the full-scale overall reduction of about 3 dB (A) is much lower than the reductions observed in *Fig.39*. This is due to the dominance of the low frequencies for the overall level. The other reduction concepts in *Fig.39* show generally smaller effects than the reversal of tail rotor sense of rotation. Note the large reduction at 500 Hz due the reduced tip speed. This causes a reduction in the overall noise level of a few dB's (*Fig.32*).

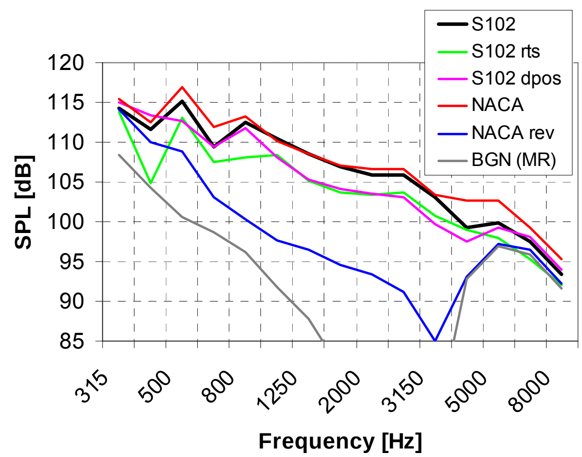

Fig.39: Integrated tail rotor noise spectra for level flight (60 m/s), showing effect of different noise reduction concepts for S102 and NACA0012 tail rotor: rts=reduced tip speed; dpos=change in TR position; rev=reversed sense of rotation; BGN=background noise (main rotor only case)

The integrated tail rotor spectra were also used to investigate the effect of the main rotor on tail rotor noise (interaction effects). The tail rotor integration contour was the same as in *Fig.38*. *Fig.40* shows an increase in tail rotor noise between 1 and 4 kHz due to the presence of the main rotor. Interestingly, a small noise reduction is observed below 500 Hz. As shown in *Fig.10*, the inflow noise contours only show a small effect of MR-TR interaction on the overall noise level. However, if we look at the inflow noise contours for individual frequency bands (*Fig. 41*), the trends are the same as in the integrated noise spectra from the array (*Fig.40*).

Fig.41 also shows the projection of the phased array surface (array position below model) on the inflow scan plane (as 'seen' from the TR position, see also *Fig.34*). These contours show that the array measures only a small part of the total noise radiation pattern.

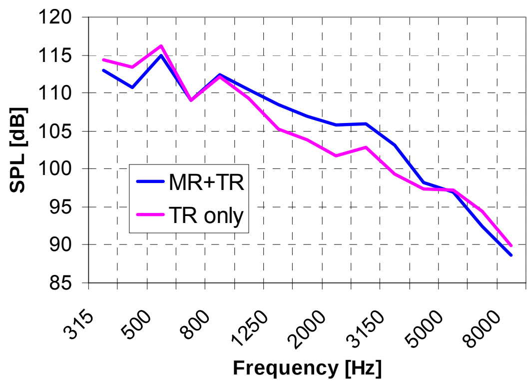

Fig.40: Integrated tail rotor noise spectra for level flight (60 m/s), showing effect of main rotor on tail rotor noise

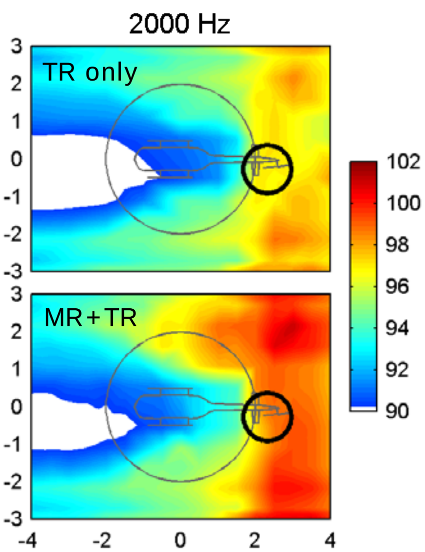

Fig.41: Inflow footprints for level flight (60 m/s), showing effect of main rotor on tail rotor noise (compare to Fig. 40). The projection of the phased array surface on the inflow plane is indicated by the black circle (array below model)

Although the processing method for rotating sources (ROSI,Ref.15) was intended for identification of noise sources on the main rotor blades (see previous section), it was also applied to cases where the tail rotor noise was dominant. Surprisingly, this yielded interesting information on the dependence of tail rotor noise on main rotor azimuth. *Fig.42* and *Fig.43* show standard source plots and ROSI plots for the level flight and climb condition respectively. For the level flight condition, the phase difference between the main and tail rotor was nearly constant during the first 30 main rotor revolutions (only the first 30 main rotor revolutions were used for the ROSI plots). For the climb condition the phase difference was varying. The circle in the ROSI plots indicates the position of the tail rotor center during the revolution of the main rotor. Since for the level flight condition the MR and TR were in phase, the tail rotor azimuth was directly coupled to the main rotor azimuth. Therefore, in *Fig.42* the positions where the tail rotor blades are horizontal can be indicated by the radial line segments (the length of the segments corresponds to the tail rotor diameter). Since the tail rotor RPM was five times higher than the main rotor RPM, and the tail rotor has two blades, there are 10 blade passages during one main rotor revolution.

The ROSI plots in *Fig.42* clearly show 10 sources, corresponding to the 10 tail rotor blade passages. Since the source radii are larger than the radius of the main rotor, the sources must be due to the tail rotor. The fact that the azimuthal source locations coincide with the line segments, shows that the tail rotor noise is produced when the blades are horizontal. Moreover, the source maxima are inside the tail rotor circle, indicating that the noise is produced by the upstream tail rotor blade. Interestingly, it can be seen that the two loudest blade passages are those where the tail rotor blade is closest to the main rotor blade. At 1.6 kHz, increased levels are also observed for the tail rotor passages directly after the passage of the other two main rotor blades. Thus, the ROSI plots clearly demonstrate the interaction between the main and tail rotor for the level flight condition, which is consistent with the results in *Fig.40* and *Fig.41*.

Fig.43 shows example ROSI plots for the climb condition. Since the phase difference between main and tail rotor was varying, there was no fixed relationship between the tail and main rotor azimuth. As a result, *Fig.43* does not show 10 sources (as in Fig. 42), but a circular noise pattern. However, it can be clearly seen that on the average the tail rotor blades produce most noise just after the passage of the main rotor blades. Thus, the ROSI plots also demonstrate interaction effects for a varying phase difference between main and tail rotor.

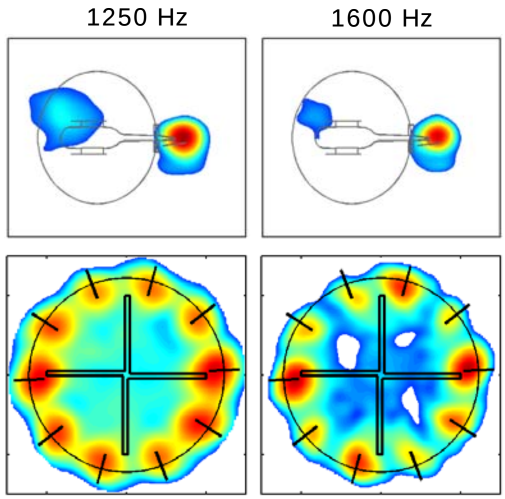

Fig.42: Standard acoustic source plots (upper row) and corresponding ROSI plots (lower row) for level flight (60 m/s).The phase difference between main and tail rotor was constant. The circle in the ROSI plots indicates the position of the TR center during rotation of the MR. The radial line segments indicate the positions where the TR blades are horizontal

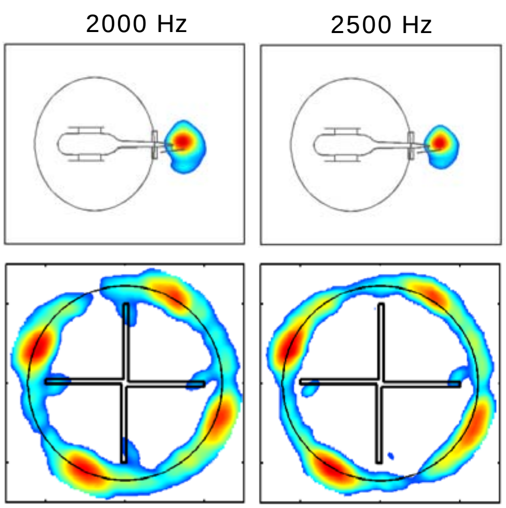

Fig.43: Standard acoustic source plots (upper row) and corresponding ROSI plots (lower row) for the climb condition. The phase difference between main and tail rotor was varying. The circle in the ROSI plots indicates the position of the TR center during rotation of the MR

5. Conclusions

A comprehensive wind tunnel study was conducted in DNW to investigate technologies for reducing noise, especially tail rotor noise and vibration of rotary wing aircraft. The test is performed under the umbrella of EU HeliNOVI project. An extensive acoustic and aerodynamic database was acquired for different MR/TR/ Fuselage configuration under different flight conditions. Also included are the test results of TR noise reduction potential through variation of blade and tip speed, through change of the tail rotor sense of rotation, and by modifying the tail rotor position. The following conclusions are drawn from the results and discussion presented:

1. Detailed investigations have confirmed that TR is major source of noise at 12° climb and 60m/s level flight while MR dominates total noise radiation during 6° descent flight; The comparison of noise level at MR/TR operation with that of isolated TR show a slight increased noise level for MR/TR operation for both climb and level flight conditions;

2. TR self BVI noise may be main source of noise radiated by TR and the level of extra BVI peaks due to interaction of MR tip vortex and TR blade is quite small; The interactions of MR tip vortex and TR blade are observed for both climb and level flight conditions, but correlation with acoustic results shows that their overall effect on tail rotor noise is small. Therefore individual interaction of TR with MR tip vortex may be second effect on noise;

3. Besides a reduction of rotor tip speed, the most efficient tail rotor noise reduction concept consists of changing the tail rotor sense of rotation from 'Advancing Side Down-ASD' to 'Advancing Side Up-ASU'. When comparing with TR in ASD mode, the noise reduction of more than 5 dBA is observed for the 12º climb and 60m/s level flight conditions. The noise reduction for new TR position is mainly due to increasing the advancing blade distance rather than changing TR aerodynamic behavior;

4. Selected results from the out-of-flow phased microphone array have illustrated the capabilities of this technique for helicopter noise. The array was utilized to determine the relative importance of main and tail rotor noise as a function of frequency, for various flight conditions. By comparing integrated tail rotor noise spectra, MR-TR interaction effects and tail rotor noise reduction concepts were assessed. Furthermore, the array provides additional information about source locations and directivity that cannot be extracted from inflow contour plots alone. It should be noted, however, that the array measures only a small part of the total noise radiation pattern. Using a

processing method for rotating sources, small noise differences between individual main rotor blades could be identified. Surprisingly, this method also clearly showed the dependence of tail rotor noise on main rotor azimuth for cases where tail rotor noise was dominant.

Acknowledgement

The HeliNovi project is generously supported by the European Union under the Competitive and Sustainable Growth Programme in the 5th Framework, Contract Nr. G4RD-CT-2001-40113.

Special thanks go to the engineers, technicians, and mechanics of DLR, DNW and NLR for their tireless efforts in preparation and conduction of this highly complex test.

The authors would like to thank Mr. Mike Pidd (QinetiQ), Mr.Jürgen Langer (DLR) and Mrs. Daniele Falchero (EC) for their comments and the revision of the language on the paper.

Reference

[1]Yu, Y., “The HART II Test - Rotor Wakes and Aeroacoustics with Higher-Harmonic Pitch Control (HHC) Inputs-The Joint German/ French/Dutch/US Project–“, 58th Annual Forum of the American Helicopter Society, Montreal, Canada, 2002.

[2] Leverton, J.W., Pollard, J.S. and Willis, C.R., “Main Rotor-Wake/ Tail Rotor Interaction“, Vertica, Vol.1, pp. 213-224, 1977.

[3] Leverton, J.W., “Reduction of Helicopter Noise by Use of a Quiet Tail Rotor“, Paper No. 24, European Rotorcraft Forum, Sept. 1980.

[4] Schultz, K.-J., Splettstoesser, W.R., “Helicopter Main Rotor/ Tail Rotor Noise Radiation Characteristics from Scaled Model Rotor Experiments in the DNW“, 49th AHS Annual Forum, St. Louis, Missouri, May 19-21, 1993.

[5] Fitzgerald, J. and Kohlepp, F., “Research Investigation of Helicopter Main Rotor/Tail Rotor Interaction Noise“, NASA CR 4143, May 1988.

[6] Martin, R.M., Burley, C.L., “Acoustic Test of a Model Rotor and Tail Rotor, Results for the Isolated Rotors and Combined Cofiguration“, NASA TM 101550, Feb. 1989.

[7] George, A.R. and Chou, S.T., “A Comparative Study of Tail Rotor Noise Mechanisms“, 41st AHS Annual Forum, Fort Worth, Texas, May 1985.

[8] Yin, J., Buchholz, H., and Splettstoesser, W., ‘Numerical Simulation of Bo105 Main/Tail Rotor Interaction Noise And Preliminary Comparisons with Flight Test Results’, 28th European Rotorcraft Forum,17 - 20 Sep. 2002, Bristol, England

[9] Oerlemans, S., and Sijtsma, P., "Acoustic Array Measurements of a 1:10.6 Scaled Airbus A340 Model", AIAA paper 2004-2924 (2004).

[10] Sijtsma, P., and Stoker, R.W., "Determination of Absolute Contributions of Aircraft Noise Components using Fly-Over Array Measurements", AIAA paper 2004-2958 (2004).

[11] Oerlemans, S., Schepers, J.G., Guidati, G., and Wagner, S., "Experimental Demonstration of Wind Turbine Noise Reduction through Optimized Airfoil Shape and Trailing-Edge Serrations", presented at the European Wind Energy Conference, Copenhagen (2001).

[12] Oerlemans, S. and Méndez López, B., "Acoustic Array Measurements on a Full Scale Wind Turbine", AIAA paper 2005-2963 (2005).

[13] Oerlemans, S., and Migliore, P., "Aeroacoustic wind tunnel tests of wind turbine airfoils", AIAA paper 2004-3042 (2004).

[14] Brooks, T.F., Marcolini, M.A., and Pope, D.S., "A directional array approach for the measurement of rotor noise source distributions with controlled spatial resolution", Journal of Sound and Vibration 112 (1987).

[15] Sijtsma, P., Oerlemans, S., and Holthusen, H., "Location of rotating sources by phased array measurements", AIAA paper 2001-2167 (2001).

[16] Langer, H.-J.; Junker, B.; Plassmeier, V.; Buchner, F.; Mikulla, V.; Mercker,E.: The Unique Capabilities of a Complete Mach-Scaled Helicopter Model for the DNW-LLF. Paper #50, 27th European Rotorcraft Forum, Moscow, 2001

[17] Langer, H.-J., Dieterich, O., Oerlemans, S., Schneider, O., Wall, B. v.d., Yin, J., “The EU HeliNOVI Project -Wind Tunnel Investigations for Noise and Vibration Reduction”, 31st European Rotorcraft Forum, Florence, Italy, 2005

[18] Holthusen, H., and Smit, H., "A new data-acquisition system for microphone array measurements in wind tunnels", AIAA paper 2001-2169 (2001).

[19] Johnson, D.H., and Dudgeon, D.E., "Array Signal Processing", Prentice Hall (1993).

[20] Amiet, R.K., "Refraction of Sound by a Shear Layer", Journal of Sound and Vibration, Vol. 58, No. 2, pp. 467-482, 1978.

[21] Heineck, J.T., Yamauchi, G.K., Woodcock, L. Laurenco, A.J., “Application of Three-Component PIV to a Hovering Rotor Wake”, 56th Annual Forum of the American Helicopter Society, Virginia Beach, VA, USA, 2000

[22] Wall, B. v.d.,, Richard, H, “Analysis Methodology for 3C PIV Data”, 31st European Rotorcraft Forum, Florence, Italy, 2005